Dynamic Modeling and Control of a Piezo-Electric Dual-Stage Tape Servo Actuator

Uwe Boettcher, Bart Raeymaekers, Raymond A. de Callafon, and Frank E. Talke

Center for Magnetic Recording Research, University of California San Diego, La Jolla, CA 92093-0401 USA

We present a data-based approach for modeling and controller design of a dual-stage tape servo actuator. Our method uses step response measurements and a generalized realization algorithm to identify a multivariable discrete-time model of the actuator. The data acquisition and modeling can be implemented in the servo firmware of a tape drive. We have designed a dual-stage controller, based on the model, using loop shaping techniques adopted for multivariable control problems. We applied the procedure to the prototype of a dual-stage actuator tape head to reduce the effect of lateral tape motion. The prototype consists of a conventional voice coil motor for coarse positioning and a micro-actuator for fine positioning. The micro-actuator, which is mounted on the voice coil motor, uses a piezo crystal to follow high-frequency lateral tape motion (up to the kilohertz regime), while the voice coil motor follows only low-frequency lateral tape motion. Compared to a single-stage design, the dual-stage servo design provides a 25% bandwidth improvement and a voice coil motor control signal that is much smaller in magnitude.

***Index Terms*—Magnetic tape recording, modeling, servosystems.**

I. Introduction

MAGNETIC tape recording has been used for digital data storage for more than 50 years. Storage capacity and areal density of data bits have been increasing exponentially in the past [1] and the price per gigabit of storage has decreased significantly over the same time. The cost per gigabit is much lower in tape storage devices than in hard disk drives [2]. A tape in a tape drive is exposed to many disturbances during reading and writing of data. Since tape is flexible, track densities are generally much lower compared to hard disk drives. To increase track density, improved track-following servo mechanisms are needed [3]. A schematic of a typical tape transport is shown in Fig. 1. The tape moves from the supply reel to the take-up reel at velocity v. Data are written on the tape and read from the tape by the read/write head. The lateral position of the tape head is determined by means of a timing based servo pattern on the magnetic tape [4] and is adjusted by a voice coil motor (VCM) for track following. The VCM rejects incoming disturbances such as lateral tape motion (LTM) which is defined as the motion of the tape perpendicular to the tape transport direction (see Fig. 1). LTM causes track misregistration and is a limiting factor in achieving track densities above 1000 tracks per inch (40 tracks per mm) [5]. Sources of LTM are imperfections of the reel motor, contacts of the tape edge with other components of the drive, and friction of the surfaces or edges of the tape with guidance elements [6]. Those disturbances occur over the whole frequency range. However, high-frequency LTM (above 500 Hz) is much smaller in magnitude than low-frequency LTM [7]. Thus, a high bandwidth servo controller is desired to reject LTM disturbances. The performance of the servo is limited in state-of-the-art drives by saturation of the control signals. To increase the track density on magnetic tape, it is necessary to improve the track following servo mechanism using improved actuator and servo control designs. The idea to include a second-stage actuator that moves a smaller inertia, and, thus, enables a higher overall servo performance was proposed for a hard disk drive (HDD) more than 15 years ago [8]. Since then, many researchers have designed, studied and implemented dual-stage actuators in HDDs using electrostatic, electromagnetic ([9]–[16]), or piezoelectric effects ([17]–[21]). Micro-actuators have been implemented mainly in experimental devices rather than commercial applications. It is anticipated that dual-stage actuators will become essential to allow further increases in track density. In order to stay competitive with HDDs, future tape drives will require track densities in excess of 30 kilo tracks per inch (ktpi). Dual-stage actuators promise to be a solution to obtain such high track densities.

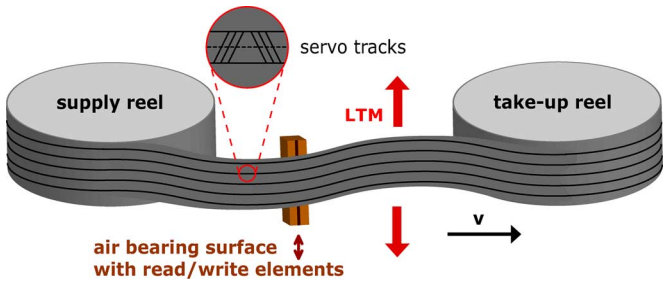

Fig. 1. Schematic of a typical tape transport.

In this study, a state-of-the-art commercially available tape head [22] was modified [23] to include a piezo-based piggyback actuator (PZT). The PZT is positioned to only actuate the air bearing surface with the read/write elements. This increases the servo bandwidth beyond 500 Hz (typically achievable only with a VCM actuator) while maintaining or even decreasing the magnitude of the control signals via frequency separation between the actuators. Consequently, low-frequency servo tracking is achieved with the VCM whereas high-frequency tracking is obtained with the PZT actuator. Hence, an overall bandwidth improvement can be achieved using appropriate control algorithms.

Manuscript received August 24, 2008; revised December 04, 2008. Current version published June 19, 2009. Corresponding author: U. Boettcher (e-mail: uwe@ucsd.edu).

Color versions of one or more of the figures in this paper are available online at http://ieeexplore.ieee.org.

Digital Object Identifier 10.1109/TMAG.2009.2015050

0018-9464/$25.00 © 2009 IEEE

Authorized licensed use limited to: Univ of Calif San Diego. Downloaded on June 19, 2009 at 14:33 from IEEE Xplore. Restrictions apply.

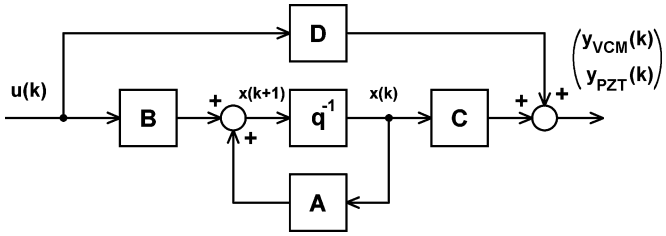

Fig. 2. State space model of dual-stage actuator.

This paper illustrates a data-based approach for the design of a multi-input, single-output (MISO) discrete time model of a dual-stage actuator. In addition, the paper implements a dual-stage controller using a MISO model and standard loop-shaping techniques based on the PQ method [24].

II. System Modeling

A. Generalized Realization Algorithm

The complexity of the mechanical system makes it difficult to derive models from first principals. Instead, experimental data are used to obtain a discrete time model using system identification techniques. The Generalized Realization Algorithm (GRA) proposed by de Callafon [25] allows the direct estimation of a discrete time model based on experimental data obtained from the input/output relationship. Specifically, this algorithm can be used to generate a multivariable model of the dual-stage actuator using simple step response measurements. Measurements of this type can be integrated in the firmware of the tape drive to facilitate the calibration of the tape servo system.

The GRA computes the state space matrices $\mathbf{A}$, $\mathbf{B}$, $\mathbf{C}$ and $\mathbf{D}$ of a multivariable model of the dual-stage actuator, illustrated in Fig. 2 where q denotes the usual discrete-time shift operator. Here, $u(k)$ represents the system input, while $y_{\mathrm{VCM}}(k)$ and $y_{\mathrm{PZT}}(k)$ represent the system output. The GRA is related to the Ho-Kalman algorithm [26] which uses the decomposition of a Hankel matrix that contains the Markov parameters (impulse response terms) of the system. However, in the present approach, step response measurements are used, representing a more realistic experimental environment than using impulse response measurements. For more details on the GRA see [25].

The input/output relationship of the system shown in Fig. 2 can be written as

$$\mathbf{Y} = \mathbf{HU} + \mathbf{E} \tag{1}$$

where $\mathbf{Y}$ is a Hankel matrix of the output signals, $\mathbf{U}$ is the input matrix, and $\mathbf{H}$ is a Hankel matrix that contains the Markov parameters $g(k)$ defined by

$$g(k) = \begin{cases} \mathbf{D} & \text{for } k = 0 \\ \mathbf{CA}^{k-1}\mathbf{B} & \text{for } k \geq 1 \end{cases} \tag{2}$$

forming the matrix

$$\mathbf{H} = \mathbf{\Gamma\Omega} \tag{3}$$

where $\mathbf{\Gamma}$ and $\mathbf{\Omega}$ are the observability and controllability matrix, respectively, defined by

$$\mathbf{\Gamma} = \begin{bmatrix} \mathbf{C} \\ \mathbf{CA} \\ \vdots \\ \mathbf{CA}^{k-1} \end{bmatrix}, \quad \mathbf{\Omega} = [\mathbf{B} \quad \mathbf{AB} \quad \cdots \quad \mathbf{A}^{k-1}\mathbf{B}]. \tag{4}$$

The matrix $\mathbf{E}$ contains the effect of past input signals multiplied by the Markov parameters of the system. Since a step-function is chosen as the input, and the system is considered to be linear and time-invariant, $\mathbf{E}$ is a row-wise listing of past output signals [25]. The key of the GRA is that a realization is performed based on the weighted Hankel matrix $\mathbf{R} = \mathbf{Y} - \mathbf{E}$, allowing the use of step function input signals instead of impulse response measurements.

The measured data are stored in a $2N \times N$ Hankel Matrix $\mathbf{Y}$

$$\mathbf{Y} = \begin{bmatrix} y_{\mathrm{v}}(1) & y_{\mathrm{v}}(2) & \cdots & y_{\mathrm{v}}(N) \\ y_{\mathrm{p}}(1) & y_{\mathrm{p}}(2) & \cdots & y_{\mathrm{p}}(N) \\ y_{\mathrm{v}}(2) & y_{\mathrm{v}}(3) & \cdots & y_{\mathrm{v}}(N+1) \\ y_{\mathrm{p}}(2) & y_{\mathrm{p}}(3) & \cdots & y_{\mathrm{p}}(N+1) \\ \vdots & \vdots & \vdots & \vdots \\ y_{\mathrm{v}}(N) & y_{\mathrm{v}}(N+1) & \cdots & y_{\mathrm{v}}(2N-1) \\ y_{\mathrm{p}}(N) & y_{\mathrm{p}}(N+1) & \cdots & y_{\mathrm{p}}(2N-1) \end{bmatrix} \tag{5}$$

where N denotes the number of data points for each measurement. The vectors y_{v} and y_{p} denote the measured step response of the VCM and the PZT, respectively. $\mathbf{E}$ can be defined by

$$\mathbf{E} = \begin{bmatrix} y_{\mathrm{v}}(0) & \cdots & y_{\mathrm{v}}(0) \\ y_{\mathrm{p}}(0) & \cdots & y_{\mathrm{p}}(0) \\ \vdots & \vdots & \vdots \\ y_{\mathrm{v}}(N-1) & \cdots & y_{\mathrm{v}}(N-1) \\ y_{\mathrm{p}}(N-1) & \cdots & y_{\mathrm{p}}(N-1) \end{bmatrix}. \tag{6}$$

The weighted Hankel matrix $\mathbf{R}$ is defined as

$$\mathbf{R} = \mathbf{Y} - \mathbf{E} = \mathbf{HU} \tag{7}$$

and has the same rank as $\mathbf{H}$. The matrix $\mathbf{R}$ is decomposed into a $2\mathrm{N} \times \mathrm{n}$ matrix $\mathbf{R_1}$ and an $\mathrm{n} \times \mathrm{N}$ matrix $\mathbf{R_2}$, by using singular value decomposition (SVD). This decomposition enables choosing the rank n, and, thus, the order of the estimated model. The SVD is applied to R as follows:

$$\mathbf{R} = U\Sigma\mathbf{V}^{\mathrm{T}} = [U_{\mathrm{n}} \quad U_{\mathrm{s}}] \begin{bmatrix} \Sigma_{\mathrm{n}} & 0 \\ 0 & \Sigma_{\mathrm{s}} \end{bmatrix} \begin{bmatrix} V_{\mathrm{n}}^{\mathrm{T}} \\ V_{\mathrm{s}}^{\mathrm{T}} \end{bmatrix} \tag{8}$$

Authorized licensed use limited to: Univ of Calif San Diego. Downloaded on June 19, 2009 at 14:33 from IEEE Xplore. Restrictions apply.

where $\mathbf{V}$ and $\mathbf{U}$ are unitary matrices, and Σ is a diagonal matrix that contains the singular values of the original matrix. The n largest singular values are stored in Σ_n while Σ_s contains the remaining smaller part. Using SVD and reducing $\mathbf{R}$ to a matrix with rank n yields

$$\mathbf{R}_{\mathrm{n}} = \mathbf{R_1}\mathbf{R_2} \tag{9}$$

where $\mathbf{R_1}$ and $\mathbf{R_2}$ are defined by

$$\mathbf{R_1} = U_{\mathrm{n}}\Sigma_{\mathrm{n}}^{1/2}, \quad \mathbf{R_2} = \Sigma_{\mathrm{n}}^{1/2}V_{\mathrm{n}}^{\mathrm{T}}. \tag{10}$$

With (4), we have $\mathbf{R_1} = \mathbf{\Gamma}$ and $\mathbf{R_2} = \mathbf{\Omega U}$, where $\mathbf{U}$ has full rank. The shifted version of $\mathbf{Y}$ is denoted by $\bar{\mathbf{Y}}$ and defined by

$$\bar{\mathbf{Y}} = \begin{bmatrix} y_{\mathrm{v}}(2) & y_{\mathrm{v}}(3) & \cdots & y_{\mathrm{v}}(N+1) \\ y_{\mathrm{p}}(2) & y_{\mathrm{p}}(3) & \cdots & y_{\mathrm{p}}(N+1) \\ y_{\mathrm{v}}(3) & y_{\mathrm{v}}(4) & \cdots & y_{\mathrm{v}}(N+2) \\ y_{\mathrm{p}}(3) & y_{\mathrm{p}}(4) & \cdots & y_{\mathrm{p}}(N+2) \\ \vdots & \vdots & \vdots & \vdots \\ y_{\mathrm{v}}(N+1) & y_{\mathrm{v}}(N+2) & \cdots & y_{\mathrm{v}}(2N) \\ y_{\mathrm{p}}(N+1) & y_{\mathrm{p}}(N+2) & \cdots & y_{\mathrm{p}}(2N) \end{bmatrix} \tag{11}$$

and the corresponding shifted version of $\mathbf{R}$ can be described as

$$\bar{\mathbf{R}} = \bar{\mathbf{Y}} - \bar{\mathbf{E}}. \tag{12}$$

From (2) and (4) it can be observed that the shifted version of $\mathbf{R}$ becomes

$$\bar{\mathbf{R}} = \mathbf{\Gamma A \Omega U} = \mathbf{R_1 A R_2}. \tag{13}$$

Since $\mathbf{R_1}$, $\mathbf{R_2}$, and $\bar{\mathbf{R}}$ are known, the state space matrix $\mathbf{A}$ can be estimated. Therefore, the left and right inverse of (10) can be defined as

$$\mathbf{R_1^*} = \Sigma_{\mathrm{n}}^{-1/2}U_{\mathrm{n}}^{\mathrm{T}}, \quad \mathbf{R_2^*} = V_{\mathrm{n}}\Sigma_{\mathrm{n}}^{-1/2} \tag{14}$$

and an estimation for the state space matrix $\mathbf{A}$ can be shown to be

$$\mathbf{A} = \mathbf{R_1^*}\bar{\mathbf{R}}\mathbf{R_2^*}. \tag{15}$$

From (4) we observe that the input matrix $\mathbf{B}$ can be described as the first column of $\mathbf{R_2}$ and that the first two rows of $\mathbf{R_1}$ form the output matrix $\mathbf{C}$

$$\mathbf{C} = \begin{bmatrix} \mathbf{C}_{\mathrm{v}} \\ \mathbf{C}_{\mathrm{p}} \end{bmatrix}. \tag{16}$$

The feed-through term $\mathbf{D}$ contains only the first data point of the two output signals after an input step, i.e.,

$$\mathbf{D} = \begin{pmatrix} \mathbf{D}_{\mathrm{v}} \\ \mathbf{D}_{\mathrm{p}} \end{pmatrix} = \begin{pmatrix} y_{\mathrm{v}}(0) \\ y_{\mathrm{p}}(0) \end{pmatrix}. \tag{17}$$

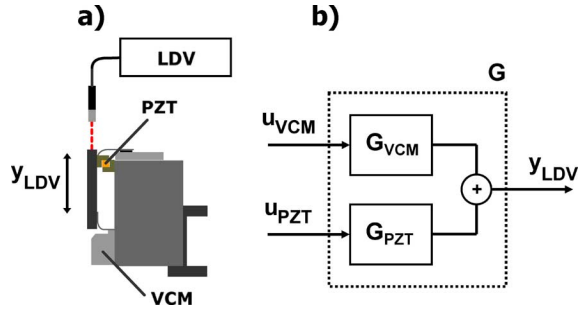

Fig. 3. (a) Schematic of the dual-stage actuator prototype and (b) dual-input single-output model.

B. Application of the GRA to the Dual-Stage Actuator Prototype

The prototype of the dual-stage actuator tape head used in this study does not have timing based servo capability. Instead, the servo mechanism is mimicked by measuring the lateral position of the air bearing surface using a laser Doppler vibrometer (LDV) with an independent timing based interrupt for data acquisition. Fig. 3(a) shows a schematic of the experimental set-up. The model of the dual-stage actuator G is shown in Fig. 3(b) where G_{VCM} and G_{PZT} represent the unknown dynamics of the VCM and the PZT, respectively. The signals u_{VCM} and u_{PZT} denote the system input whereas y_{LDV} denotes the system output, which is the position of the air bearing surface. With the state space model depicted in Fig. 2 and the separation of the $\mathbf{C}$ and $\mathbf{D}$ matrix in (16) and (17), the dynamics G_{VCM} and G_{PZT} will be represented by the discrete-time models

$$\begin{aligned} G_{\mathrm{VCM}}(q) &= \mathbf{D}_{\mathrm{v}} + \mathbf{C}_{\mathrm{v}}(q\mathbf{I} - \mathbf{A})^{-1}\mathbf{B} \\ G_{\mathrm{PZT}}(q) &= \mathbf{D}_{\mathrm{p}} + \mathbf{C}_{\mathrm{p}}(q\mathbf{I} - \mathbf{A})^{-1}\mathbf{B} \end{aligned} \tag{18}$$

indicating common poles of G_{VCM} and G_{PZT}. In (18), $\mathbf{I}$ denotes the identity matrix.

To achieve the desired lateral displacement of the air bearing surface by using the full range of the D/A converter, a voltage driver is used to operate the micro-actuator. In addition, a current driver is used to actuate the voice coil motor. The velocity output of the LDV provides the output data to estimate the discrete time models of both the micro-actuator and voice coil motor. The data are sampled at 1 MHz to avoid aliasing, and time-based averaging minimizes the effect of noise disturbances during the system identification phase. After downsampling to 20 kHz, the first $N = 450$ datapoints were considered for the model estimation. The discrete-time models G_{VCM} and G_{PZT} will be modeled at a sampling frequency of 20 kHz. The servo controller will be implemented at the same sampling frequency in real-time.

C. Model Validation

Using the GRA, one can obtain a plot of the singular values of $\mathbf{R}$ (Fig. 4). Based on Fig. 4 and time and frequency domain model validation, the model order can be chosen to be high enough to capture most of the common system dynamics of both, the VCM and the PZT actuator as indicated in (18).

Authorized licensed use limited to: Univ of Calif San Diego. Downloaded on June 19, 2009 at 14:33 from IEEE Xplore. Restrictions apply.

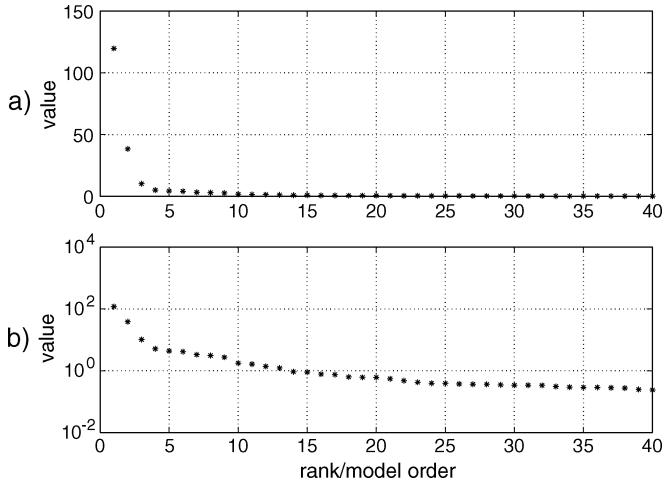

Fig. 4. Singular values of $\mathbf{R}$ in (a) linear and (b) logarithmic scale.

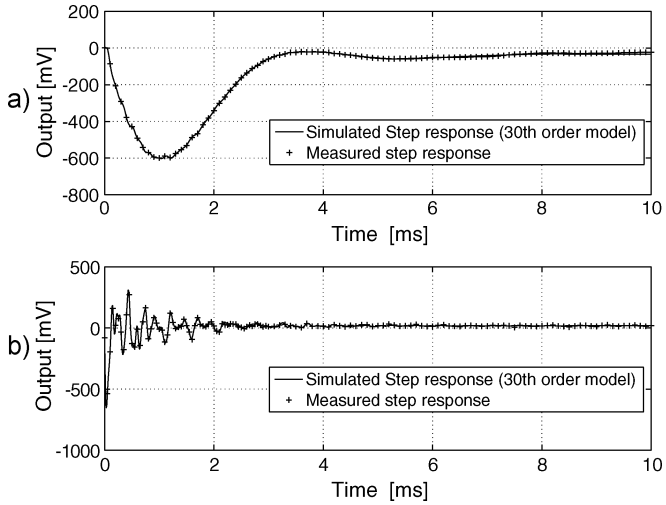

Fig. 5. Time domain validation using step response data for (a) voice coil motor model $G_{\mathrm{VCM}}(q)$ and (b) micro-actuator model $G_{\mathrm{PZT}}(q)$.

From Fig. 4, any model with order larger than 20 will suffice. However, to ensure that all the resonance modes relevant for control design are captured, we chose an order of 30, allowing also a good fit of the small resonance mode around 2 kHz. The 30th order model was validated in two different ways. First, the model is used to simulate an input step which is compared to the actual step response measurement. The result of this time domain validation is depicted in Fig. 5. Excellent agreement is observed between the simulated and measured step response data. Fig. 5(a) shows the results for the voice coil motor and Fig. 5(b) shows the results for the micro-actuator.

To investigate the effectiveness of the proposed GRA method, the model is validated in the frequency domain by measuring the frequency response functions (FRF) of both the VCM and the micro-actuator using a dynamic signal analyzer. Fig. 6(a) shows the results for the voice coil motor and Fig. 6(b) shows the results for the micro-actuator. It is observed that very good agreement exists between the measured FRF and the estimated model and that almost all high-frequency resonance modes are captured. The VCM model shows also a low-frequency stiffness that is related to the leaf springs that are included in the mechanical design of the VCM.

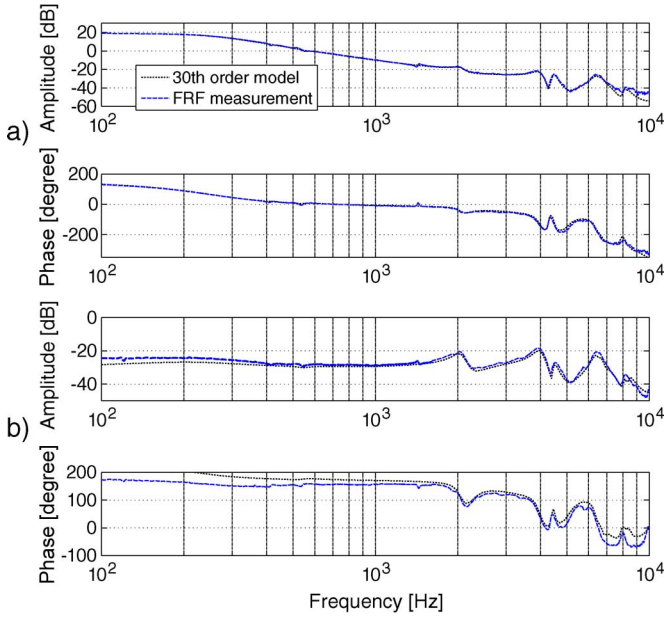

Fig. 6. Frequency domain validation (a) voice coil motor and (b) micro-actuator.

III. Dual-Stage Controller Design

A. PQ-Method

The relative motion between the two actuators of a dual-stage actuator tape head is unknown, i.e., only one position measurement is available to determine the lateral position of the air bearing surface. Thus, the system is a dual-input single-output system (DISO). Many different control design techniques for dual-stage actuators have been developed. An overview of applied control techniques is given in [10]. The servo control structure for the dual-stage actuator tape head is shown in Fig. 7. The position error signal PES is the difference between the desired lateral position of the tape head r and the actual lateral position of the tape head y. C_{VCM} and C_{PZT} are the VCM and micro-actuator controllers. G_{VCM} and G_{PZT} represent the dynamics of both actuators. The controller design is based on the PQ method which was first proposed in [24] and applied to a dual stage controller in hard disk drives in [27]. The PQ method allows to decompose a dual-input single-output system into two single-input single-output systems and addresses interactions between the actuators by means of frequency separation. The VCM and the PZT counteract each other at the zeros of G_{SISO} which is the parallel structure of both actuators illustrated in Fig. 7 and defined as

$$G_{\mathrm{SISO}} = C_{\mathrm{VCM}} \cdot G_{\mathrm{VCM}} + C_{\mathrm{PZT}} \cdot G_{\mathrm{PZT}}. \tag{19}$$

The main idea behind the PQ method is the observation that the zeros of the model of G_{SISO} in (19) are equivalent to the poles of the feedback connection shown in Fig. 8 where P and Q are defined by

$$P(q) = \frac{G_{\mathrm{VCM}}(q)}{G_{\mathrm{PZT}}(q)} \quad \text{and} \quad Q(q) = \frac{C_{\mathrm{VCM}}(q)}{C_{\mathrm{PZT}}(q)}. \tag{20}$$

Authorized licensed use limited to: Univ of Calif San Diego. Downloaded on June 19, 2009 at 14:33 from IEEE Xplore. Restrictions apply.

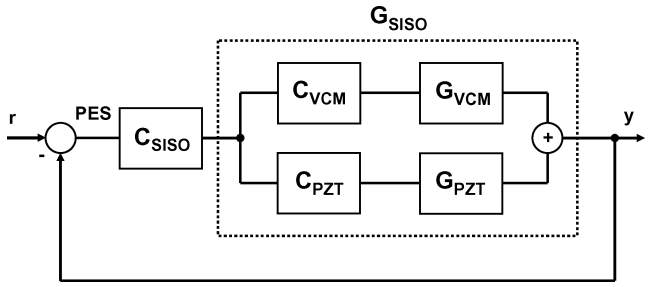

Fig. 7. Dual-stage actuator tape head control design.

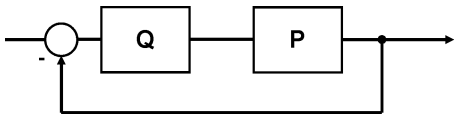

Fig. 8. PQ method.

The model of the plant $P(q)$ and the compensator $Q(q)$ is used to place the closed-loop zeros of the feedback-connection depicted in Fig. 7. As indicated in (18), the multivariable state space model of the dual-stage actuator has a common $\mathbf{A}$- and $\mathbf{B}$-matrix. Hence, the computation of P is found by the standard matrix manipulation

$$\begin{aligned} \bar{x}(k+1) &= \bar{\mathbf{A}}\bar{x}(k) + \bar{\mathbf{B}}y_{\mathrm{p}}(k) \\ y_{\mathrm{v}}(k) &= \bar{\mathbf{C}}\bar{x}(k) + \bar{\mathbf{D}}y_{\mathrm{p}}(k) \end{aligned} \tag{21}$$

where the new input and output of the system is represented by $y_{\mathrm{p}}(k)$ and $y_{\mathrm{v}}(k)$, respectively. The state space matrices of P are defined by

$$\begin{aligned} \bar{\mathbf{A}} &= \mathbf{A} - \mathbf{B}\mathbf{D}_{\mathrm{p}}^{-1}\mathbf{C}_{\mathrm{p}} \\ \bar{\mathbf{B}} &= \mathbf{B}\mathbf{D}_{\mathrm{p}}^{-1} \\ \bar{\mathbf{C}} &= \mathbf{C}_{\mathrm{v}} - \mathbf{D}_{\mathrm{v}}\mathbf{D}_{\mathrm{p}}^{-1}\mathbf{C}_{\mathrm{p}} \\ \bar{\mathbf{D}} &= \mathbf{D}_{\mathrm{v}}\mathbf{D}_{\mathrm{p}}^{-1} \end{aligned} \tag{22}$$

where $\mathbf{A}$, $\mathbf{B}$, $\mathbf{C}_{\mathrm{v}}$, $\mathbf{C}_{\mathrm{p}}$, $\mathbf{D}_{\mathrm{v}}$ and $\mathbf{D}_{\mathrm{p}}$ are the state space matrices given in (18).

After defining P, a controller Q for the feedback connection shown in Fig. 8 is designed. The stability of this feedback connection guarantees stability for the parallel structure described in (19) and allows consideration of the dashed box in Fig. 7 as a single-input single-output system. Frequency separation is achieved via closed-loop zero placement. Finally, the controller C_{SISO} is designed to ensure stability of the overall system and to achieve desired bandwidth requirements.

B. Application of the PQ Method to the Model of a Dual-Stage Actuator

Q and therefore C_{VCM} and C_{PZT} can be parameterized using

$$C_{\mathrm{VCM}}(q) = K_{\mathrm{VCM}}\frac{(q-a_1)}{(q-1)}\cdot\frac{(q^2-b_1q-b_2)}{(q^2-c_1q-c_2)} \tag{23}$$

and

$$C_{\mathrm{PZT}}(q) = K_{\mathrm{PZT}}\cdot\frac{(q-1)}{(q-d_1)} \tag{24}$$

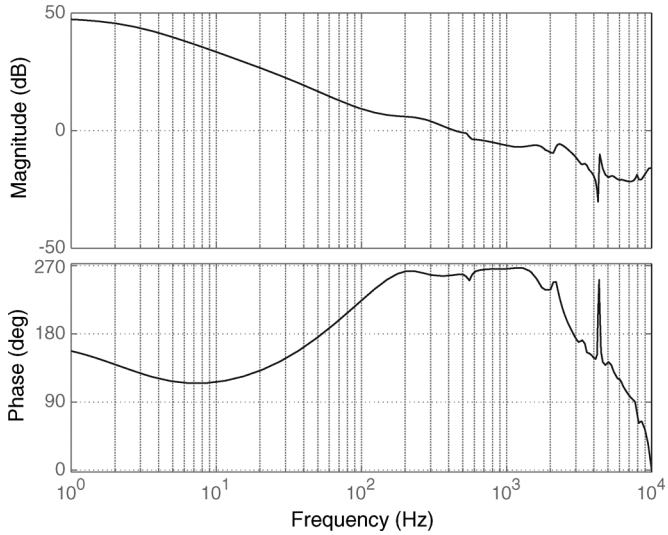

Fig. 9. Bode response of open loop gain of $P(q)\cdot Q(q)$.

where K_{VCM}, K_{PZT}, a_1, b_1, b_2, c_1, c_2 are free design parameters.

In the parameterization of (23), the VCM controller C_{VCM} contains an integrator to remove the steady-state error and reject steady-state disturbances. A second order lead compensator increases the phase margin and ensures stability in the feedback loop. The micro-actuator controller given in (24) is designed as a high pass filter, since it only needs to respond to high-frequency disturbances due to LTM above several hundred Hertz. Using standard root locus techniques, one can optimize the parameters of (23) and (24) for phase and gain margin leading to $K_{\mathrm{VCM}} = 1$, $K_{\mathrm{PZT}} = 7.43$, $a_1 = 0.8966$, $b_1 = 1.9374$, $b_2 = -0.9384$, $c_1 = 1.3100$, $c_2 = -0.6289$, $d_1 = 0.7789$ for the specific dual-stage actuator considered in this paper.

Fig. 9 shows the open loop Bode diagram of the loop gain $P\cdot Q$. The PZT dominates the response above the 0 dB crossover frequency, the VCM responds below that frequency.

The controller C_{SISO} is designed to handle the closed-loop stability and performance of the overall system. Notch filters were used to suppress high-frequency resonance modes seen in the dual-stage actuator model.

Due to the small mass of the piezo-based actuator, it is possible to cancel high-frequency resonance modes. Cancellation of these modes for a single-stage controller requires large control signals. We used the design freedom in C_{SISO} to demonstrate this effect by providing additional cancellation of high-frequency resonance modes at the expense of a higher controller order. In particular, C_{SISO} was chosen to be a 16th order filter. Fig. 10 shows the open loop transfer function of both actuators. The transfer function of the overall system $C_{\mathrm{SISO}}\cdot G_{\mathrm{SISO}}$ can be obtained by combining the transfer functions of the VCM and the micro-actuator, i.e., $C_{\mathrm{SISO}}\cdot G_{\mathrm{SISO}} = C_{\mathrm{SISO}}\cdot C_{\mathrm{VCM}}\cdot G_{\mathrm{VCM}} + C_{\mathrm{SISO}}\cdot C_{\mathrm{PZT}}\cdot G_{\mathrm{PZT}}$ As a final test on the evaluation of the dual-stage controller, the frequency separation obtained with the dual-stage controller can be illustrated by simulating the individual displacement of both actuators. The results are shown in Fig. 11. It can be observed that the VCM moves to the desired position slowly, while the micro-actuator acts fast and

Authorized licensed use limited to: Univ of Calif San Diego. Downloaded on June 19, 2009 at 14:33 from IEEE Xplore. Restrictions apply.

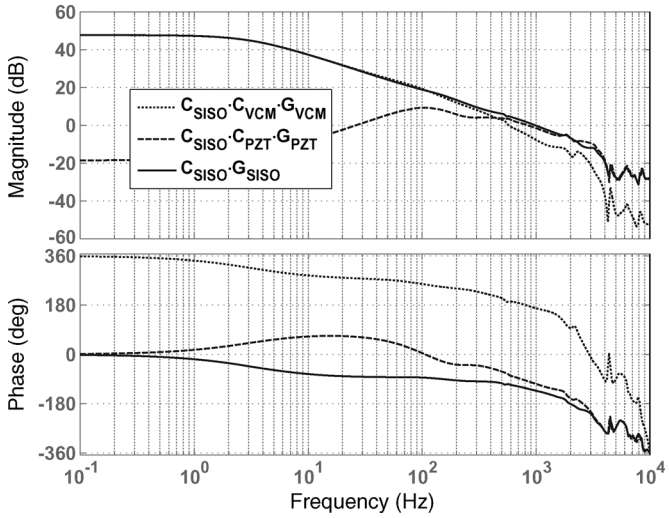

Fig. 10. Bode response of open loop transfer functions.

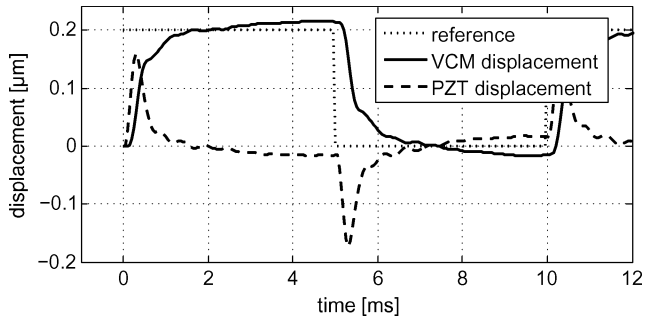

Fig. 11. Simulation of step response of dual-stage actuator illustrating frequency separation.

moves back to its zero position, since there is no DC component in the control signal for the micro-actuator.

C. Comparison With Single-Stage Control Design

To illustrate the improvement of the dual-stage servo system, a comparison of the performance of the dual-stage controller to a single-stage controller $C_{\rm ss}$ that only uses the voice coil motor has been done. For reference, the transfer function of $C_{\rm ss}(q)$ is given in (25) and it was designed to achieve maximum closed-loop bandwidth.

$$C_{\rm ss}=\frac{-6.745\cdot(q^2-1.922q+0.928)(q^2-1.555q+0.947)}{(q-0.999)(q-0.214)(q-0.1)(q^2-1.515q+0.926)}. \tag{25}$$

The parameterization is similar to the one for $C_{\rm VCM}$ but uses an additional notch filter to suppress the resonance mode in the actuator dynamics at 2 kHz.

To measure the control signal level required to attain a pre-determined bandwidth, it is useful to compute the maximum norm (Tschebyschew norm) of the control signal $u_{\rm VCM}(t)$ sent to the VCM due to a step change in reference for track following. The control signal $u_{\rm VCM}(t)$ of a standard single-stage servo system is given by

$$u_{\rm VCM}(t)=\frac{C_{\rm ss}(q)}{1+G_{\rm VCM}(q)C_{\rm ss}(q)}r(t) \tag{26}$$

TABLE I
SYSTEM PARAMETERS

	Single-stage	Dual-stage
gain margin	6 dB	6.8 dB
phase margin	42 degrees	48 degrees
overshoot	33%	21%
5% settling time	1.1 ms	0.8 ms
closed loop bandwidth	≈ 800 Hz	≈ 1 kHz
VCM control signal level $\|u_{\rm VCM}\|_\infty$	0.675 V	0.142 V

whereas for the dual-stage control system, the input signal to the VCM is given by

$$u_{\rm VCM}(t) = \frac{C_{\rm SISO}(q)C_{\rm VCM}(q)}{1+C_{\rm SISO}(q)\left[C_{\rm PZT}(q)G_{\rm PZT}(q)+C_{\rm VCM}(q)G_{\rm VCM}(q)\right]}r(t). \tag{27}$$

From (27) it can be observed that the effect of the micro-actuator is added to the denominator, and, thus yields a lower VCM control signal compared to the single-stage controller depicted in (26). The maximum norm for the VCM control signal is defined by

$$\|u_{\rm VCM}\|_\infty=\max_t|u_{\rm VCM}(t)| \quad \text{for } r(t)=\begin{cases}0.2\,\mu{\rm m} & t>0\\ 0\,\mu{\rm m} & t\le 0\end{cases}. \tag{28}$$

Given the maximum VCM control signal as one performance measure, Table I compares the dual-stage and the single-stage design. At the same time, standard performance measures such as gain and phase margin, overshoot, settling time and bandwidth are taken into account. The sensitivity function (error rejection function) of both the single-stage and dual-stage controller are shown in Fig. 12. From Fig. 12, we observe that the single-stage controller design has a better disturbance rejection at frequencies below 240 Hz, while the dual-stage controller has a better disturbance rejection above that frequency. In addition, it can be seen that the small mass of the piezo-based actuator allows better reduction of high-frequency resonance modes as indicated earlier.

The closed loop bandwidth of the dual-stage design shows an improvement of approximately 25% compared to the single-stage design. In addition, it can be observed that the level of the control signal of the dual-stage actuator is much smaller than that of the single-stage actuator. In particular, the maximum magnitude of the control signal of the VCM in the dual-stage design is about 20% of the control signal level in the single-stage design, for the same displacement.

The inputs to both the VCM and the PZT are constrained. A 5 V input constraint for the VCM (mimics the actual current constraint) and a 30 V input constraint for the PZT is defined. The simulation results are illustrated in Fig. 13. Here, Fig. 13(a) shows the lateral position of the tape head for a 2 μm step response, while Fig. 13(b) shows the magnitude of the control signal. The solid line and the dashed line represent the dual-stage and single-stage controller, respectively. The dotted line shows the reference signal r, i.e., the desired lateral position of the tape head. The single-stage VCM controller hits

Authorized licensed use limited to: Univ of Calif San Diego. Downloaded on June 19, 2009 at 14:33 from IEEE Xplore. Restrictions apply.

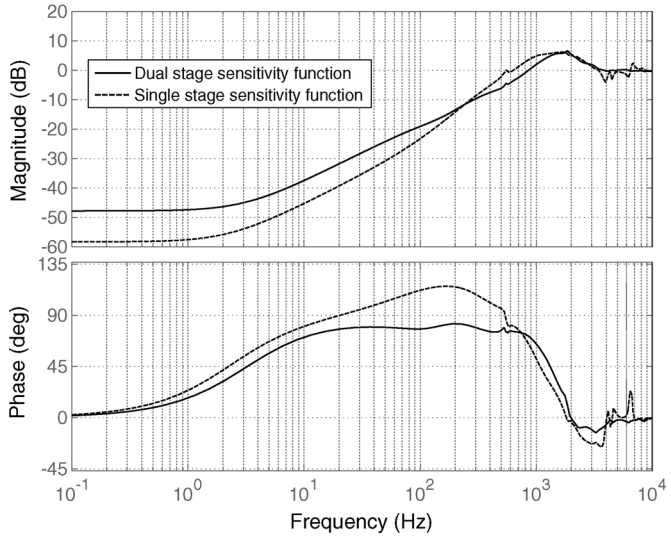

Fig. 12. Sensitivity function of single-stage and dual-stage controller design.

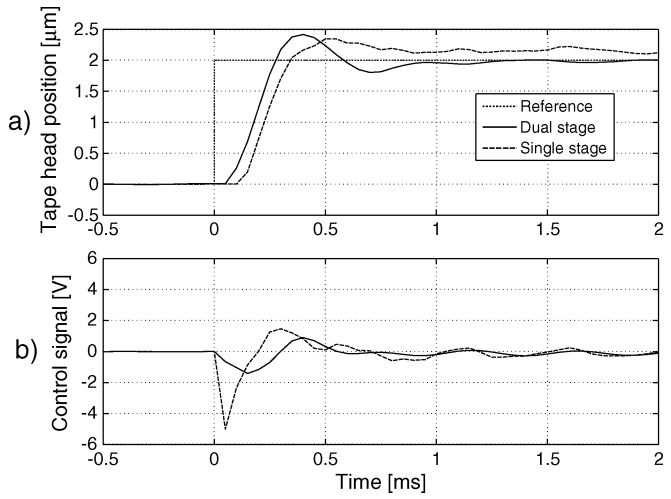

Fig. 13. Simulated step response for dual-stage and single-stage control design.

the 5 V constraint which increases the settling time whereas the VCM control signal stays below 1.5 V. The maximum value of the PZT control signal (not illustrated) is about 21 V. Hence, the dual-stage controller can reject high-frequency disturbances with larger amplitudes than the single-stage controller, using the same control signal level.

In addition, we simulated the PES using a non-repeatable filtered band pass disturbance between 200 Hz and 3 kHz, representing the LTM, entering the feedback system. Taking into account the same saturation limits of the control signals of the actuators (5 V and 30 V), we can simulate the PES and the results are depicted in Fig. 14. This figure shows how the high-frequency disturbances cause control signal saturation for the VCM in the single-stage design, while the VCM control signals are much smaller in the dual-stage design. We also observe a 21% improvement in the 3-sigma level of the PES, and a 28% improvement in the maximum absolute value of the PES, indicating an improvement of the track misregistration budget.

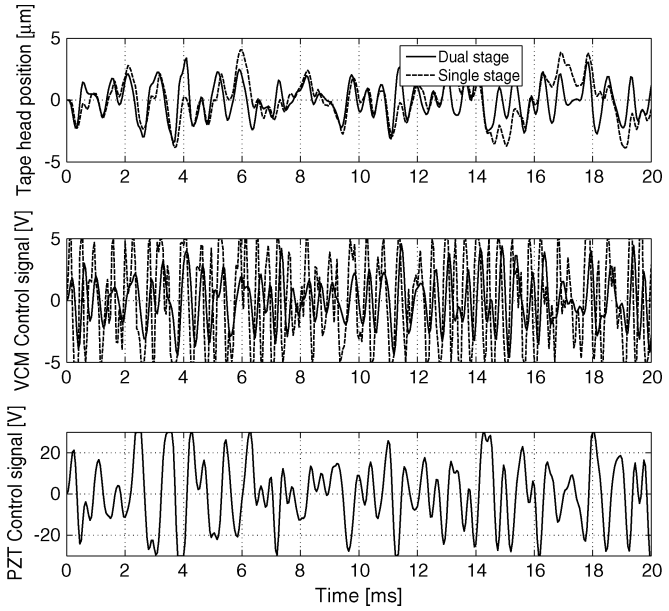

Fig. 14. Simulated PES using non-repeatable filtered band pass disturbance.

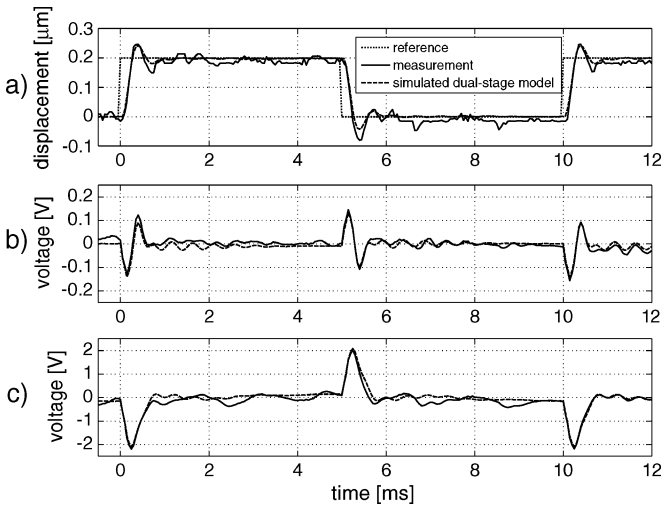

Fig. 15. Implemented controller.

IV. Controller Implementation

The dual-stage controller was implemented in the dual-stage actuator tape head prototype. A 100 Hz square wave of 0.2 μm amplitude was applied as a reference signal. Fig. 15 shows the results. Fig. 15(a) shows the lateral tape head position; Fig. 15(b) shows the control signal for the voice coil motor; Fig. 15(c) shows the control signal for the micro-actuator. From Fig. 15, it can be observed that the dual-stage controller settles the lateral position of the tape head to the desired (reference) position within less than 1 ms. The simulated output signal and the two simulated control signals are in very good agreement with the measurements.

V. Discussion and Conclusion

An algorithm that uses step-response measurements for modeling of the dual-stage actuator has been proposed in this paper. Simple SISO controller design techniques were used to design

Authorized licensed use limited to: Univ of Calif San Diego. Downloaded on June 19, 2009 at 14:33 from IEEE Xplore. Restrictions apply.

a dual-stage controller for a dual-stage actuator tape head. The controller was implemented as a prototype. The dual-stage design uses a much smaller control signal for the VCM actuator than a comparable single-stage design. Thus, it enables rejection of disturbances with larger amplitudes. The estimated model shows an excellent agreement with the measured results.

Furthermore, an improvement in the closed loop bandwidth was achieved. However, since the first peak in the FRF of the micro-actuator was close to the maximum achievable closed-loop bandwidth of the VCM, this improvement was small. The mechanical design of the prototype could be altered to yield a stiffer second stage. A higher stiffness would move some of the low-frequency resonance modes of the frequency response function to a higher frequency, and, thus, would allow a larger closed loop bandwidth.

ACKNOWLEDGMENT

The authors would like to thank Prof. J. Lienig from Dresden University of Technology for his collaboration and interest in this work.

REFERENCES

[1] D. B. Richards and M. P. Sharrock, "Key issues in the design of magnetic tapes for linear systems of high track density," *IEEE Trans. Magn.*, vol. 34, pp. 1878–1882, 1998.

[2] E. R. Childers, W. Imaino, J. H. Eaton, G. A. Jaquette, P. V. Koeppe, and D. J. Hellman, "Six orders of magnitude in linear tape technology: The one-terabyte project," *IBM J. Res. Develop.*, vol. 47, no. 4, pp. 471–482, 2003.

[3] R. H. Dee, "Magnetic tape: The challenge of reaching hard-disk-drive data densities on flexible media," *MRS Bull.*, vol. 31, pp. 404–408, 2006.

[4] R. C. Barrett, E. H. Klaassen, T. R. Albrecht, G. A. Jacquette, and J. H. Eaton, "Timing-based track-following servo for linear tape systems," *IEEE Trans. Magn.*, vol. 34, no. 4, pp. 1872–1877, Jul. 1998.

[5] J. Jose, R. J. Taylor, R. A. de Callafon, and F. E. Talke, "Characterization of lateral tape motion and disturbances in the servo position error signal of a linear tape drive," *Tribol. Int.*, vol. 38, pp. 625–632, 2005.

[6] R. J. Taylor and F. E. Talke, "Investigation of roller interactions with flexible tape medium," *Tribol. Int.*, vol. 38, pp. 599–605, 2005.

[7] B. Raeymaekers and F. E. Talke, "Lateral motion of an axially moving tape on a cylindrical guide surface," *J. Appl. Mech.*, vol. 74, pp. 1053–1056, 2007.

[8] K. Mori, T. Munemoto, H. Otsuki, Y. Yamaguch, and K. Akagi, "A dual stage magnetic disk drive actuator using a piezoelectric device for a high track density," *IEEE Trans. Magn.*, vol. 27, no. 6, pp. 5298–5300, Nov. 1991.

[9] N. Afzulpurkar and Y. Weerakamhaeng, "Precision positioning using MEMS based microactuator," *Mechatronics*, vol. 12, pp. 1213–1223, 2002.

[10] R. Horowitz, Y. Li, K. Oldham, S. Kon, and X. Huang, "Dual-stage servo systems and vibration compensation in computer hard disk drives," *Contr. Eng. Pract.*, vol. 15, pp. 291–305, 2007.

[11] X. Huang, R. Horowitz, and Y. Li, "Track-following control with active vibration damping and compensation of a dual-stage servo system," *Microsyst. Technol.*, vol. 11, pp. 1276–1286, 2005.

[12] T. Hirano, L.-S. Fan, W. Y. Lee, J. Hong, W. Imaino, S. Pattanaik, S. Chan, P. Webb, R. Horowitz, S. Aggarwal, and D. A. Horsley, "High-bandwidth high-accuracy rotary microactuators for magnetic hard disk drive tracking servos," *IEEE/ASME Trans. Mech.*, vol. 3, no. 3, pp. 156–165, 1998.

[13] L.-S. Fan, H. H. Ottesen, T. C. Reiley, and R. W. Wood, "Magnetic recording head positioning at very high track densities using a microactuator-based, two-stage servo system," *IEEE Trans. Ind. Electron.*, vol. 42, no. 3, pp. 222–233, 1995.

[14] D. A. Horsley, N. Wongkomet, R. Horowitz, and A. P. Pisano, "Precision positioning using a microfabricated electrostatic actuator," *IEEE Trans. Magn.*, vol. 35, no. 2, pp. 993–999, Mar. 1999.

[15] T. Semba, T. Hirano, J. Hongt, and L. Fan, "Dual-stage servo controller for HDD using MEMS microactuator," *IEEE Trans. Magn.*, vol. 35, no. 5, pp. 2271–2273, Sep. 1999.

[16] C. C. Chung, C. W. Seo, and S.-H. Lee, "Two degree-of-freedom dual-stage actuator controller design for hard disk drives," *IEEE Trans. Magn.*, vol. 36, no. 5, pp. 2255–2257, Sep. 2000.

[17] Y. Li, F. Marcassa, R. Horowitz, R. Oboe, and R. Evans, "Track-following control with active vibration damping of a PZT-actuated suspension dual-stage servo system," *ASME J. Dyn. Syst., Meas., Contr.*, vol. 128, pp. 568–576, 2006.

[18] R. A. de Callafon, R. Nagamune, and R. Horowitz, "Robust dynamic modeling and control of dual-stage actuators," *IEEE Trans. Magn.*, vol. 42, no. 2, pp. 247–254, Feb. 2006.

[19] S. Koganezawa, Y. Uematsu, T. Yamada, H. Nakano, J. Inoue, and T. Suzuki, "Dual-stage actuator system for magnetic disk drives using a shear mode piezoelectric microactuator," *IEEE Trans. Magn.*, vol. 35, no. 2, pp. 988–992, Mar. 1999.

[20] S. Nakamura, H. Numasato, K. Sato, M. Kobayashi, and I. Naniwa, "A push-pull multi-layered piggyback PZT actuator," *Microsyst. Technol.*, vol. 8, pp. 149–154, 2002.

[21] R. B. Evans, J. S. Griesbach, and W. C. Messner, "Piezoelectric microactuator for dual stage control," *IEEE Trans. Magn.*, vol. 35, no. 2, pp. 977–982, Mar. 1999.

[22] R. G. Biskeborn and J. H. Eaton, "Hard-disk-drive technology flat heads for linear tape recording," *IBM J. Res. Develop.*, vol. 47, no. 4, pp. 385–400, 2003.

[23] B. Raeymaekers, M. R. Graham, R. A. de Callafon, and F. E. Talke, "Design of a dual stage actuator tape head width high bandwidth track-following capability," in *Proc. ASME Information Storage and Processing Systems Conf.*, Santa Clara, CA, 2007.

[24] S. J. Schroeck and W. C. Messner, "On controller design for linear time-invariant dual-input single-output systems," in *Proc. Amer. Contr. Conf.*, San Diego, CA, 1999.

[25] R. A. de Callafon, "Estimating parameters in a lumped parameter system with first principle modeling and dynamic experiments," in *Proc. 13th IFAC Symp. System Identification*, Rotterdam, The Netherlands, 2003, pp. 1613–1618.

[26] R. E. Kalman and B. L. Ho, "Effective construction of linear state-variable models from input/output functions," *Regelungstechnik*, vol. 14, pp. 545–548, 1966.

[27] M. Graham, R. J. M. Oosterbosch, and R. A. de Callafon, "Fixed order PQ-control design method for dual stage instrumented suspension," in *Proc. IFAC Congr.*, Praha, Czech Republic, 2005.

Authorized licensed use limited to: Univ of Calif San Diego. Downloaded on June 19, 2009 at 14:33 from IEEE Xplore. Restrictions apply.